Hyperfine-Shifted C-13 and N-15 NMR Signals from Clostridium pasteurianum Rubredoxin: Extensive Assignments and Quantum Chemical Verification

Hyperfine-Shifted ¹³C and ¹⁵N NMR Signals from *Clostridium pasteurianum* Rubredoxin: Extensive Assignments and Quantum Chemical Verification

I-Jin Lin,[†] Bin Xia,[†,‡] David S. King,[§] Timothy E. Machonkin,[‖,⊥] William M. Westler,[#] and John L. Markley*,[†,‖,#]

Graduate Program in Biophysics, Department of Biochemistry, and National Magnetic Resonance Facility at Madison, University of Wisconsin-Madison, 433 Babcock Drive, Madison, Wisconsin, 53706

Received July 16, 2009; E-mail: markley@nmrfam.wisc.edu

Abstract: Stable isotope-labeling methods, coupled with novel techniques for detecting fast-relaxing NMR signals, now permit detailed investigations of paramagnetic centers of metalloproteins. We have utilized these advances to carry out comprehensive assignments of the hyperfine-shifted ¹³C and ¹⁵N signals of the rubredoxin from *Clostridium pasteurianum* (*Cp*Rd) in both its oxidized and reduced states. We used residue-specific labeling (by chemical synthesis) and residue-type-selective labeling (by biosynthesis) to assign signals detected by one-dimensional ¹⁵N NMR spectroscopy, to nitrogen atoms near the iron center. We refined and extended these ¹⁵N assignments to the adjacent carbonyl carbons by means of one-dimensional ¹³C[¹⁵N] decoupling difference experiments. We collected paramagnetic-optimized SuperWEFT ¹³C[¹³C] constant time COSY (SW-CT-COSY) data to complete the assignment of ¹³C signals of reduced *Cp*Rd. By following these ¹³C signals as the protein was gradually oxidized, we transferred these assignments to carbons in the oxidized state. We have compared these assignments with hyperfine chemical shifts calculated from available X-ray structures of *Cp*Rd in its oxidized and reduced forms. The results allow the evaluation of the X-ray structural models as representative of the solution structure of the protein, and they provide a framework for future investigation of the active site of this protein. The methods developed here should be applicable to other proteins that contain a paramagnetic center with high spin and slow electron exchange.

Introduction

Iron−sulfur proteins are ubiquitous and essential to life.[1−3] In addition to their functional roles as electron transport proteins in photosynthesis and respiration, iron−sulfur proteins also are involved in nitrogen fixation, gene regulation, detoxification, and chemical sensing. Recently, iron−sulfur proteins have been found to play roles in human diseases, such as Parkinson's disease and Friedreich's ataxia. Oxidative inactivation of mitochondrial aconitase may play an important role in dopaminergic neuron damage in Parkinson disease.[4] The progressive neurodegenerative disease, Friedreich's ataxia, has been linked to dysfunction of the iron protein frataxin, which is thought to function in iron homeostasis and iron−sulfur protein biogenesis.[5−8]

Rubredoxin, whose redox active site consists of a single iron ligated by four cysteinyl sulfurs, is the simplest and most extensively studied iron−sulfur protein, with published investigations by NMR,[9−16] EPR,[17,18] MCD,[18,19] and Mössbauer[18,20] spectroscopies, X-ray crystallography,[21−23] and theoretical calculations.[13,14,24−26] Rubredoxin has served as a model system

† Graduate Program in Biophysics.
‡ Howard Hughes Medical Institute, University of California, Berkeley, CA 94720.
§ Present address: Beijing NMR Center, Peking University, Beijing, China.
‖ Department of Biochemistry.
⊥ Present address: Department of Chemistry, Whitman College, Hall of Science 338, 345 Boyer Ave., Walla Walla, WA 99362.
National Magnetic Resonance Facility at Madison.

(1) Beinert, H. *J. Biol. Inorg. Chem.* **2000**, *5*, 2−15.
(2) Beinert, H.; Holm, R. H.; Munck, E. *Science* **1997**, *277*, 653−659.
(3) Imsande, J. *Plant Physiol. Biochem.* **1999**, *37*, 87−97.
(4) Liang, L. P.; Patel, M. *J. Neurochem.* **2004**, *90*, 1076−1084.
(5) Puccio, H.; Koenig, M. *Curr. Opin. Genet. Dev.* **2002**, *12*, 272−277.
(6) Stehling, O.; Elsasser, H. P.; Bruckel, B.; Muhlenhoff, U.; Lill, R. *Hum. Mol. Genet.* **2004**, *13*, 300730 15.
(7) Zhang, Y.; Lyver, E. R.; Knight, S. A.; Lesuisse, E.; Dancis, A. *J. Biol. Chem.* **2005**, *280*, 19794−19807.
(8) Adinolfi, S.; Iannuzzi, C.; Prischi, F.; Pastore, C.; Iametti, S.; Martin, S. R.; Bonomi, F.; Pastore, A. *Nat. Struct. Mol. Biol.* **2009**, *16*, 390−396.
(9) Phillips, W. D.; McDonald, C. C.; Stombaugh, N. A.; Orme-Johnson, W. H. *Proc. Natl. Acad. Sci. U.S.A.* **1974**, *71*, 140−143.
(10) Prantner, A. M.; Volkman, B. F.; Wilkens, S. J.; Xia, B.; Markley, J. L. *J. Biomol. NMR* **1997**, *10*, 411−412.
(11) Volkman, B. F.; Prantner, A. M.; Wilkens, S. J.; Xia, B.; Markley, J. L. *J. Biomol. NMR* **1997**, *10*, 409−410.
(12) Volkman, B. F.; Wilkens, S. J.; Lee, A. L.; Xia, B.; Westler, W. M.; Beger, R.; Markley, J. L. *J. Am. Chem. Soc.* **1999**, *121*, 4677−4683.
(13) Wilkens, S. J.; Xia, B.; Volkman, B. F.; Weinhold, F.; Markley, J. L.; Westler, W. M. *J. Phys. Chem. B* **1998**, *102*, 8300−8305.
(14) Wilkens, S. J.; Xia, B.; Weinhold, F.; Markley, J. L.; Westler, W. M. *J. Am. Chem. Soc.* **1998**, *120*, 4806−4814.
(15) Xia, B.; Westler, W. M.; Cheng, H.; Meyer, J. P.; Moulis, J. M.; Markley, J. L. *J. Am. Chem. Soc.* **1995**, *117*, 5347−5350.
(16) Xia, B.; Wilkens, S. J.; Westler, W. M.; Markley, J. L. *J. Am. Chem. Soc.* **1998**, *120*, 4893−4894.

for investigations of the role of the metal in protein folding and assembly of the metal center.[27−31] Miniaturized rubredoxins have been designed that successfully incorporated a tetrahedrally coordinated iron.[32] Moreover, systematic site-specific mutagenesis studies have generated information about sequence effects on reduction potentials,[33−38] thermal stability,[28] and hydrogen bonding.[39,40]

Paramagnetic NMR has been proven to be of great use in studying iron−sulfur proteins.[41−45] Although the paramagnetism of the iron in all oxidation states broadens NMR signals and complicates their detection and analysis, these signals, if they can be resolved and assigned, provide detailed information about electron−nuclear interactions that control the properties of the iron center. To date, multiple approaches have taken advantage of paramagnetic effects as a means to determine the electronic and geometric structure of the iron center.[42,46] Proteins containing iron centers with fast electron relaxation, such as high-potential iron−sulfur proteins (HiPIPs), are amenable to conventional NMR experiments.[47−49] However, these methods fail with proteins containing iron centers with slow electron relaxation, such as [2Fe−2S] ferredoxins and rubredoxin. The high-spin character of the center ($S = {}^5/_2$ for Fe^{III} and $S = 2$ for Fe^{II}) makes NMR spectroscopy of rubredoxin more challenging than that of ferredoxin, whose two irons are antiferromagnetically coupled[50] ($S = 0$ for the oxidized state and $S = {}^1/_2$ for the reduced state).

Previous work from this laboratory demonstrated that the NMR protocols standard for diamagnetic proteins fail in the case of the rubredoxin from *Clostridium pasteurianum* (*Cp*Rd). For example, the $^1H-^{15}N$ heteronuclear single quantum correlation (HSQC) spectrum of oxidized *Cp*Rd lacks signals from 22 residues and that of reduced *Cp*Rd lacks signals from 12 residues.[10,11] The 12 missing signals map to the two loops that contain the cysteine residues that ligate the iron. Each metal-binding loop contains a CXXCGX motif ($C_6T_7V_8C_9G_{10}Y_{11}$ and $C_{39}P_{40}L_{41}C_{42}G_{43}V_{44}$ in *Cp*Rd). In each loop, three backbone amide amides (from residue Val8, Cys9, Tyr11 or L41, Cys42, Val44 in *Cp*Rd) donate H-bonds to cysteinyl S^γ atoms ligated to the iron. The covalent bonds to the metal and the network of $H^N \cdots S^\gamma$ H-bonds provide avenues for delocalization of unpaired electrons from the iron. These electron−nuclear interactions are responsible for the paramagnetic NMR effects: hyperfine chemical shifts, fast nuclear spin relaxation, and very broad lines. In 1998, Bertini and co-workers solved an NMR solution structure of reduced *Cp*Rd (PDB code: 1BFY).[51] Although the NMR pulse programs they used were optimized for paramagnetic signals, they failed to resolve and assign resonances from these loops. We present here nearly complete assignments of the ^{13}C and ^{15}N signals from the iron-binding loops of *Cp*Rd in its oxidized and reduced forms and compare these with hyperfine shifts calculated from the available X-ray structures. These validated assignments provide a resource for future structure−function investigations of *Cp*Rd, and the approaches used can serve as a model for investigations of other highly paramagnetic protein systems.

Materials and Methods

The procedures used for protein expression, *in vitro* iron reconstitution and purification were those previously described.[15]

Isotopic Labeling. Uniform labeling of *Cp*Rd with ^{15}N and/or ^{13}C was achieved by growing cells on standard M9 media supplemented with of $^{15}NH_4Cl$ and/or ^{13}C-glucose (Cambridge Isotope Laboratories, Andover, MA). Two strategies were used to assign signals to amino acid types: residue-type-selective labeling and inverse-residue-type-selective-labeling.[15] In the former, an excess of the labeled amino acid (Cambridge Isotope Laboratories) was added at the time of induction to M9 medium containing a mixture of all amino acids at natural abundance; in the latter, cells

(17) Borger, B.; Suter, D. *J. Chem. Phys.* **2001**, *115*, 9821–9826.

(18) Yoo, S. J.; Meyer, J.; Achim, C.; Peterson, J.; Hendrich, M. P.; Munck, E. *J. Biol. Inorg. Chem.* **2000**, *5*, 475–487.

(19) Bennett, D. E.; Johnson, M. K. *Biochim. Biophys. Acta* **1987**, *911*, 71–80.

(20) Rao, K. K.; Evans, M. C.; Cammack, R.; Hall, D. O.; Thompson, C. L.; Jackson, P. J.; Johnson, C. E. *Biochem. J.* **1972**, *129*, 1063–1070.

(21) Adman, E.; Watenpaugh, K. D.; Jensen, L. H. *Proc. Natl. Acad. Sci. U.S.A.* **1975**, *72*, 4854–4858.

(22) Bau, R.; Rees, D. C.; Kurtz, D. M.; Scott, R. A.; Huang, H. S.; Adams, M. W. W.; Eidsness, M. K. *J. Biol. Inorg. Chem.* **1998**, *3*, 484–493.

(23) Day, M. W.; Hsu, B. T.; Joshua-Tor, L.; Park, J. B.; Zhou, Z. H.; Adams, M. W. W.; Rees, D. C. *Protein Sci.* **1992**, *1*, 1494–1507.

(24) Bair, R. A.; Goddard, W. A., III *J. Am. Chem. Soc.* **1978**, *100*, 5669–5676.

(25) Grottesi, A.; Ceruso, M. A.; Colosimo, A.; Di Nola, A. *Proteins* **2002**, *46*, 287–294.

(26) Vondrasek, J.; Bendova, L.; Klusak, V.; Hobza, P. *J. Am. Chem. Soc.* **2005**, *127*, 2615–2619.

(27) Bonomi, F.; Iametti, S.; Kurtz, D. M.; Ragg, E. M.; Richie, K. A. *J. Biol. Inorg. Chem.* **1998**, *3*, 595–605.

(28) Bonomi, F.; Fessas, D.; Iametti, S.; Kurtz, D. M., Jr.; Mazzini, S. *Protein Sci.* **2000**, *9*, 2413–2426.

(29) Dauter, Z.; Wilson, K. S.; Sieker, L. C.; Moulis, J. M.; Meyer, J. P. *Proc. Natl. Acad. Sci. U.S.A.* **1996**, *93*, 8836–8840.

(30) Maher, M.; Cross, M.; Wilce, M. C.; Guss, J. M.; Wedd, A. G. *Acta Cryst. D: Biol. Cryst.* **2004**, *60*, 298–303.

(31) Moura, I.; Teixeira, M.; LeGall, J.; Moura, J. J. *J. Inorg. Biochem.* **1991**, *44*, 127–139.

(32) Lombardi, A.; Marasco, D.; Maglio, O.; Di Costanzo, L.; Nastri, F.; Pavone, V. *Proc. Natl. Acad. Sci. U.S.A.* **2000**, *97*, 11922–11927.

(33) Ayhan, M.; Xiao, Z. G.; Lavery, M. J.; Hamer, A. M.; Nugent, K. W.; Scrofani, S. D. B.; Guss, M.; Wedd, A. G. *Inorg. Chem.* **1996**, *35*, 5902–5911.

(34) Eidsness, M. K.; Burden, A. E.; Richie, K. A.; Kurtz, D. M.; Scott, R. A.; Smith, E. T.; Ichiye, T.; Beard, B.; Min, T. P.; Kang, C. H. *Biochemistry* **1999**, *38*, 14803–14809.

(35) Kummerle, R.; Zhuang-Jackson, H. Y.; Gaillard, J.; Moulis, J. M. *Biochemistry* **1997**, *36*, 15983–15991.

(36) Park, I. Y.; Eidsness, M. K.; Lin, I. J.; Gebel, E. B.; Youn, B.; Harley, J. L.; Machonkin, T. E.; Frederick, R. O.; Markley, J. L.; Smith, E. T.; Ichiye, T.; Kang, C. *Proteins* **2004**, *57*, 618–625.

(37) Xiao, Z.; Maher, M. J.; Cross, M.; Bond, C. S.; Guss, M.; Wedd, A. G. *J. Biol. Inorg. Chem.* **2000**, *5*, 75–84.

(38) Zeng, Q. D.; Smith, E. T.; Kurtz, D. M.; Scott, R. A. *Inorg. Chim. Acta* **1996**, *242*, 245–251.

(39) Lin, I. J.; Gebel, E. B.; Machonkin, T. E.; Westler, W. M.; Markley, J. L. *J. Am. Chem. Soc.* **2003**, *125*, 1464–1465.

(40) Lin, I. J.; Gebel, E. B.; Machonkin, T. E.; Westler, W. M.; Markley, J. L. *Proc. Natl. Acad. Sci. U.S.A.* **2005**, *102*, 14581–14586.

(41) Bertini, I.; Capozzi, F.; Luchinat, C.; Piccioli, M.; Vicens Oliver, M. *Inorg. Chim. Acta* **1992**, *198−200*, 483–491.

(42) Bertini, I.; Turano, P.; Vila, A. J. *Chem. Rev.* **1993**, *93*, 2833–2932.

(43) Cheng, H.; Markley, J. L. *Annu. Rev. Biophys. Biomol. Struct.* **1995**, *24*, 209–237.

(44) Machonkin, T. E.; Markley, J. L. In *Encyclopedia of Nuclear Magnetic Resonance: Supplementary Volume*; John Wiley & Sons, Ltd: New York, 2002; pp 384−401.

(45) Machonkin, T. E.; Westler, W. M.; Markley, J. L. *Inorg. Chem.* **2005**, *44*, 779–797.

(46) Bertini, I.; Luchinat, C.; Parigi, G. *Concepts Magn. Reson.* **2002**, *14*, 259–286.

(47) Bertini, I.; Briganti, F.; Luchinat, C.; Scozzafava, A.; Sola, M. *J. Am. Chem. Soc.* **1991**, *113*, 1237–1245.

(48) Bertini, I.; Capozzi, F.; Ciurli, S.; Luchinat, C.; Messori, L.; Piccioli, M. *J. Am. Chem. Soc.* **1992**, *114*, 3332–3340.

(49) Banci, L.; Bertini, I.; Capozzi, F.; Carloni, P.; Ciurli, S.; Luchinat, C.; Piccioli, M. *J. Am. Chem. Soc.* **1993**, *115*, 3431–3440.

(50) Palmer, G.; Dunham, W. R.; Fee, J. A.; Sands, R. H.; Iizuka, T.; Yonetani, T. *Biochim. Biophys. Acta* **1971**, *245*, 201–207.

(51) Bertini, I.; Kurtz, D. M., Jr.; Eidsness, M. K.; Liu, G. H.; Luchinat, C.; Rosato, A.; Scott, R. A. *J. Biol. Inorg. Chem.* **1998**, *3*, 401–410.

producing the protein were grown in the uniform-labeling medium, and the natural abundance amino acid was added in excess at the time of induction.

Rubredoxin 54mers incorporating specifically labeled residues were synthesized by standard FMOC chemistry on an ABI 431 synthesizer (Applied Biosystems, Foster City, CA) employing DCC/HOBT (*N,N*′-dicyclohexylcarbodiimide 1-hydroxybenzotriazol) activation with 3 h coupling times. They were cleaved and deprotected with reagent K, and purified by reversed-phase HPLC on a C18 column. Purity of the final product (>90%) was assessed by ESI-quadrupole mass spectrometry. The peptides were constituted with iron and purified as described previously[15] to yield [15N-Gly10]-*Cp*Rd, [15N-Val44]-*Cp*Rd, and [13C,15N-Cys9]-*Cp*Rd.

Unless specified otherwise, the NMR samples contained 4−8 mM protein, 50 mM phosphate buffer, and 10% 2H2O to provide the NMR lock signal. The pH was adjusted to 6.0, and the sample temperature was regulated at 298 K.

NMR Spectroscopy. One-dimensional (1D) 15N NMR spectra were collected on Bruker (Billerica, MA) DMX-500 and DMX-400 MHz spectrometers with Bruker 5-mm and 10-mm multinuclear broadband probes, respectively. 1D 13C NMR spectra were collected on a Bruker DMX-500 MHz spectrometer with a Bruker 5-mm QNP probe, switchable for 19F, 31P, and 13C. To suppress the diamagnetic signals and enhance the sensitivity of the paramagnetic signals, a one-pulse sequence with a short repetition time or a SuperWEFT pulse sequence was applied.[52]

13C[15N] difference decoupled spectra were collected on a Bruker DMX-600 MHz spectrometer with a custom-made 10-mm 13C[1H, 15N] probe. A 13C NMR spectrum of the carbonyl region with 15N decoupling at an empty part of the nitrogen spectrum was subtracted from one with selective decoupling at the frequency one of the hyperfine-shifted amide 15N resonances. The peak showing up in the difference spectrum was assigned to the carbonyl covalently bonded to nitrogen corresponding to the irradiated peak.[53]

13C[13C] constant time correlation spectroscopy (CT-COSY) data were collected on a Bruker DMX-500 MHz spectrometer with a Bruker 5-mm QNP probe. For diamagnetic signals, the constant time delay was set to 8 ms. For paramagnetic signals, a SuperWEFT element (180-*τ*-90) was inserted in front of the CT-COSY pulse sequence to suppress the diamagnetic signals. In this SW-CT-COSY experiment, the constant time delay was set to 4 ms to avoid the loss of rapidly relaxing signals.[54]

The redox titration experiment was performed by stepwise addition under anaerobic conditions of sodium dithionite to the NMR sample. The NMR tube was sealed to prevent sample oxidation. To accelerate the self-exchange rate between FeII- and FeIII-*Cp*Rd, the sample contained 1 M NaCl and the sample temperature was held at 303 K.

Quantum Chemical Calculations. The hyperfine shift computations utilized a 209-atom model derived from the 1.5 Å crystal structure of reduced *Cp*Rd (PDB code 1FHM[55]) and for a 1.2 Å crystal structure of oxidized *Cp*Rd (PDB code 5RXN). A structure with an alternative conformation for residue 41 in the reduced protein was also used in the calculations. Coordinates were extracted from the crystal structures for the two heptapeptides at the metal site (residues 5−11 and 38−44), including all backbone and side chain heavy atoms and the iron atom. The N-termini were capped in silico with acetyl groups, and the C-termini were capped with N-methyl groups. DS ViewerPro 5.0 from Accelrys Inc. was used to add hydrogens atoms to the reduced structure, except in the case of the structure of oxidized *Cp*Rd which included proton coordinates. The B3LYP/6-311 g** level of theory in Gaussian 03 was
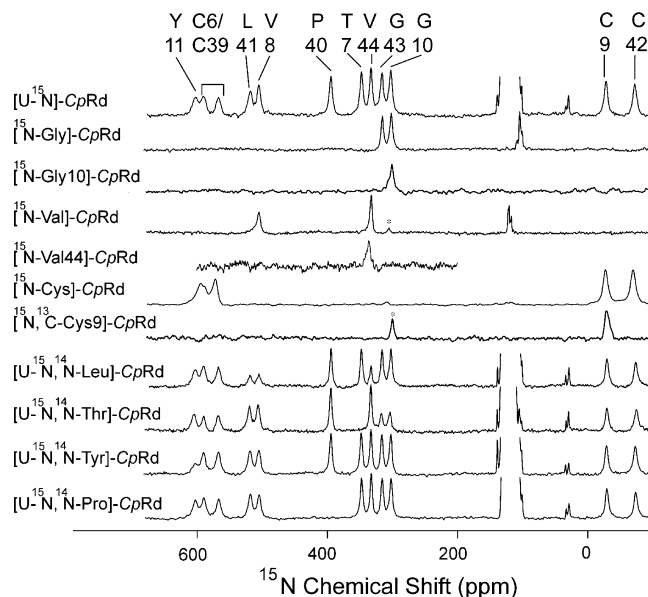
Figure 1. 1D 15N NMR spectra of uniformly and selectively 15N-labeled FeIII-*Cp*Rd. The sample contained 4−8 mM protein, 50 mM potassium phosphate buffer, and 10% 2H2O; the pH was 6.0, and the temperature was 298 K. Uniformly 15N-labeled *Cp*Rd is abbreviated as [U−15N]-*Cp*Rd. Glycine specific 15N-labeled *Cp*Rd is abbreviated as [15N-Gly]-*Cp*Rd. Inverse leucine specific 15N-labeled *Cp*Rd is abbreviated as [U−15N,14N-Leu]-*Cp*Rd. Peaks labeled with "*" originate from natural abundance 15N14N from air. Assignments are indicated above the spectrum at the top of the figure.

used in calculating the theoretical chemical shifts. The spin densities were extracted and converted to shifts in ppm by using eqs 9 and 10 from a previous publication.[14] Mean diamagnetic chemical shifts from the BMRB were used in comparing the experimentally observed chemical shifts with the computed hyperfine shifts by adding the BMRB values to the computed hyperfine shifts. All computations were performed on a 12-processor SGI Altix 3000 computer.

Results

Assignments of Amide Nitrogen Peaks. Residue-type-selective 15N labeling (and reverse labeling) led to the classification of the hyperfine-shifted 15N NMR signals of oxidized and reduced *Cp*Rd by residue type. Twelve 15N hyperfine shifts were observed in the 1D 15N spectrum of uniformly 15N-labeled *Cp*Rd in the oxidized state (Figure 1): 10 of these signals were shifted to higher frequencies (downfield), and 2 of these signals were shifted to lower frequencies (upfield). The two iron-ligating hexapeptides presumed to give rise to these signals contain residues of seven types: We produced samples of selectively labeled *Cp*Rd corresponding to three of these amino acids: [15N-Gly]-*Cp*Rd, [15N-Val]-*Cp*Rd, and [15N-Cys]-*Cp*Rd, and we produced samples of inverse selectively labeled *Cp*Rd corresponding to the remaining four: [U−15N,14N-Leu]-*Cp*Rd, [U−15N,14N-Thr]-*Cp*Rd, [U−15N,14N-Tyr]-*Cp*Rd, and [U−15N,14N-Pro]-*Cp*Rd. Although the labeling specificity was imperfect (partial transfer of the 15N label from Leu to Val and Thr to Gly were the worst cases), this approach led to the identification of all 15N hyperfine shifts by residue type and to sequence-specific assignments for resonances from the four amino acid types represented only once in the two hexapeptides (Thr7, Tyr11, Pro40, and Leu41). The eight remaining resonances correspond to amino acid types represented more than once: Cys at four sites, Gly at two sites, and Val at two sites. 15N NMR spectra of two of the three chemically synthesized rubredoxins ([15N-
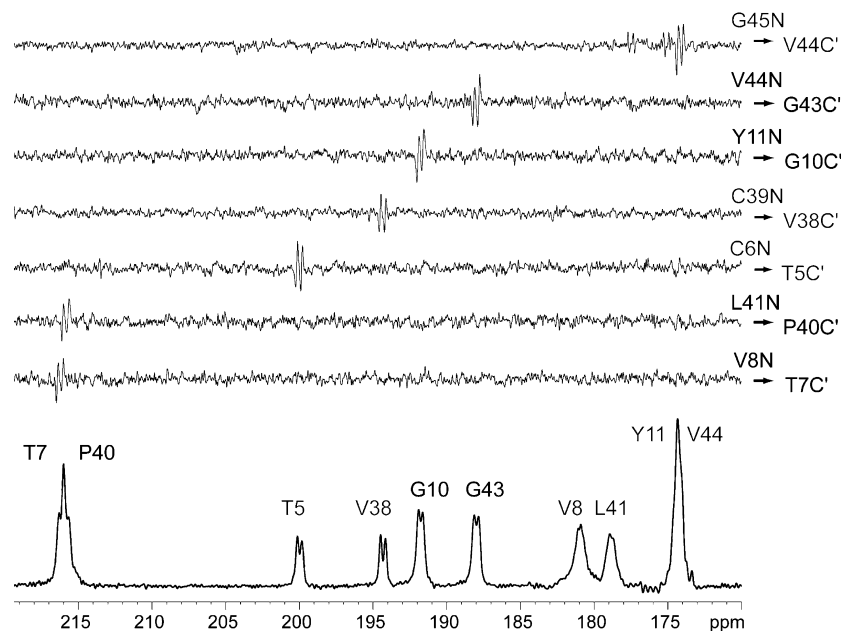
(52) Inubushi, T.; Becker, E. D. *J. Magn. Reson.* **1983**, *51*, 128–133.
(53) Jain, N. U.; Pochapsky, T. C. *Biochem. Biophys. Res. Commun.* **1999**, *258*, 54–59.
(54) Machonkin, T. E.; Westler, W. M.; Markley, J. L. *J. Am. Chem. Soc.* **2002**, *124*, 3204–3205.
(55) Min, T.; Ergenekan, C. E.; Eidsness, M. K.; Ichiye, T.; Kang, C. *Protein Sci.* **2001**, *10*, 613–621.

Figure 2. Comparison of ^{13}C[^{15}N] difference decoupling spectra of reduced [U−^{15}N,U−^{13}C]-*Cp*Rd with the 1D ^{13}C SuperWEFT spectrum of the same sample (bottom). The sample contained 4−8 mM protein, 50 mM potassium phosphate buffer, and 10% ^{2}H$_2$O; the pH was 6.0, and the temperature was 298 K. The irradiated assigned ^{15}N atoms are listed to the right of the spectra. The resulting ^{13}C′ assignments are shown on the spectrum at the bottom. The peaks labeled in black were unambiguously assigned by this ^{13}C[^{15}N] difference coupling experiment. Assignments of the peaks labeled in gray required further information from 2D NMR experiments.

Gly10]-*Cp*Rd and [^{15}N-Val44]-*Cp*Rd) (Figure 1) led to sequence-specific assignments for the ^{15}N signals of Gly10 and Gly43 and Val8 and Val44. Previous quantum chemical calculations based on the X-ray structure of *Cp*Rd predicted low-frequency (high-field) hyperfine shifts for Cys9 and Cys42 and high-frequency (low-field) hyperfine shifts for Cys6 and Cys39. Thus the ^{15}N NMR spectrum of the third chemically synthesized rubredoxin, [^{15}N-Cys9]-*Cp*Rd (Figure 1), both confirmed this expectation and provided sequence-specific assignments for the two low-frequency cysteine peaks.

Assignments of Hyperfine-Shifted Carbon-13 Signals. Ten hyperfine-shifted signals, tentatively assigned to carbonyl carbons, were observed in the 1D ^{13}C spectrum of [U−^{15}N,U−^{13}C]-*Cp*Rd in the reduced state, a spectrum in which diamagnetic signals were removed by the SuperWEFT pulse sequence (Figure 2). The prior assignments of backbone ^{15}N signals were extended to the directly bonded carbonyl ^{13}C by means of selective decoupling difference spectroscopy. Because the nitrogen hyperfine signals are well resolved, it was possible to selectively irradiate an individual ^{15}N$_{i+1}$ peak so as to decouple its interaction with the adjacent ^{13}C′$_i$. This led to a change in the line shape of the carbonyl carbon in the spectrum with the decoupler on resonance but not in the spectrum with the decoupler off resonance.[56] Thus, the signal observed in the difference spectrum identifies ^{13}C′$_i$. In the case of reduced *Cp*Rd, irradiation of the amide nitrogen atoms from Val8, Leu41, Tyr11, and Val44 clearly identified, respectively, the chemical shifts of the carbonyl carbons from residues Thr7, Pro40, Gly10, and Gly43 (Figure 2). Although irradiation of the ^{15}N signal from Gly45 gave rise to multiple signals in the ^{13}C[^{15}N] difference spectrum, owing to the known presence of diamagnetic Gly ^{15}N signals in this region,[10] the carbonyl carbon of Val44 at 175 ppm was identified in the difference spectrum.

Because of the remaining ambiguity in the nitrogen assignments for Cys6 and Cys39, the carbonyl carbon resonances of Thr5 and Val38 could be identified and correlated with ^{15}N signals but not assigned individually.

In the conventional ^{13}C[^{13}C] CT-COSY spectrum, signals from paramagnetic residues were found to be weak or undetected (Figure 3A). By using paramagnetic-optimized ^{13}C[^{13}C] SW-CT-COSY,[54] diamagnetic signals were suppressed, and the intensities of the paramagnetic signals were increased (Figure 3B). Although Thr5 and Val38 are not located on the metal-binding loops, their carbonyl carbons experience hyperfine shifts to high frequency. Nevertheless, signals from these carbonyl carbons appeared in the conventional ^{13}C[^{13}C] CT-COSY spectrum but were not present in the paramagnetic-optimized ^{13}C[^{13}C] SW-CT-COSY spectrum. This indicates that Thr5 and Val38 experience minimal paramagnetic line broadening. Side chain ^{13}C−^{13}C connectivities were found that linked these carbonyl signals to others in the carbon spin system (Figure 3A) and allowed their identification by residue type (threonine for the signal at low frequency and valine for the signal at high frequency). These identifications made it possible to distinguish the signals from the two spin pairs identified by ^{13}C[^{15}N] difference decoupling: Thr5-^{13}C′-Cys6-^{15}N and Val38-^{13}C′-Cys39-^{15}N. This led, in turn, to residue-specific assignments for the previously ambiguously assigned carbonyl carbons of Thr5 and Val38 and amide nitrogens of Cys6 and Cys39.

Signals from Pro40, Thr7, Gly10, Gly43, Tyr11, and Val44, which were weak in the conventional ^{13}C[^{13}C] CT-COSY spectrum (Figure 3A), were well resolved in the paramagnetic-optimized ^{13}C[^{13}C] SW-CT-COSY spectrum (Figure 3B). The residue types of Pro40, Thr7, Gly10 and Gly43, identified from side-chain ^{13}C−^{13}C connectivities, agreed with the assignments from the ^{13}C[^{15}N] difference decoupling experiments. The carbonyl signals from Tyr11 and Val44, which were unresolved in the 1D ^{13}C spectrum, were seen to have distinct frequencies

(56) Cheng, H.; Westler, W. M.; Xia, B.; Oh, B. H.; Markley, J. L. *Arch. Biochem. Biophys.* **1995**, *316*, 619–634.
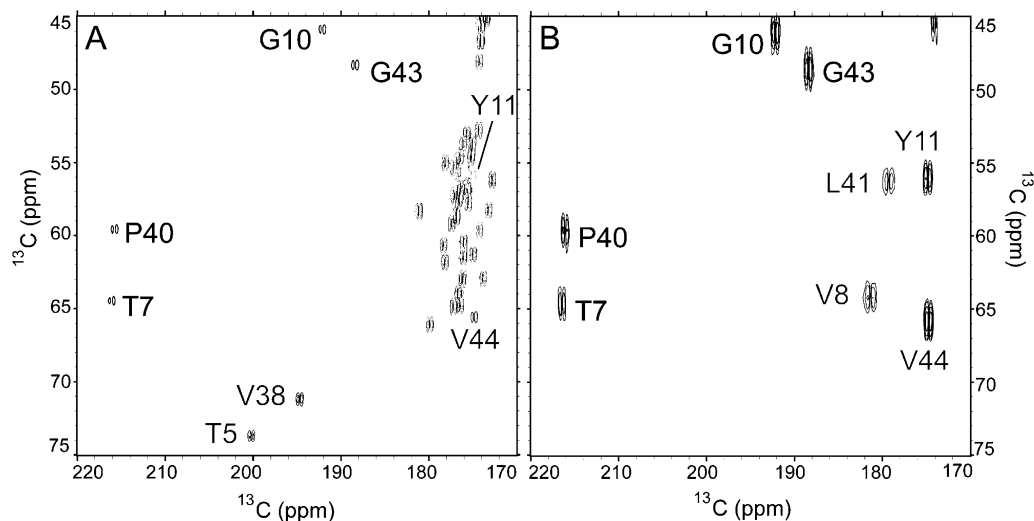
Figure 3. Spectra of reduced [U−^{15}N,U−^{13}C]-*Cp*Rd. The sample contained 4−8 mM protein, 50 mM potassium phosphate buffer, and 10% ^2H_2O; the pH was 6.0, and the temperature was 298 K. (A) Conventional $^{13}C[^{13}C]$ CT-COSY. (B) Paramagnetic-optimized $^{13}C[^{13}C]$ SW-CT-COSY. Peaks labeled in black were assigned by $^{13}C[^{15}N]$ difference coupling experiments alone. The assignments were subsequently confirmed by side chain $^{13}C–^{13}C$ connectivity from 2D $^{13}C[^{13}C]$ spectra. Peaks labeled in gray were assigned by combining results from $^{13}C[^{15}N]$ difference coupling experiments and 2D $^{13}C[^{13}C]$ spectra.

in the indirect dimension of the 2D $^{13}C[^{13}C]$ SW-CT-COSY spectrum; these $^{13}C−^{13}C$ connectivities led to their unambiguous assignment.

Two weak carbonyl signals appeared in the paramagnetic-optimized $^{13}C[^{13}C]$ SW-CT-COSY spectrum (Figure 3B) but not in the $^{13}C[^{13}C]$ CT-COSY spectrum (Figure 3A). Although the carbonyl carbon signals were very weak, their $^{13}C−^{13}C$ connectivities could be traced in the spectrum and used to identify one spin system as valine and the other as leucine. These two signals were assigned to the carbonyl carbons of Val8 and Leu41, the only two residues left unassigned.

This strategy of using $^{13}C[^{15}N]$ difference decoupling and paramagnetic-optimized $^{13}C[^{13}C]$ SW-CT-COSY experiments, which worked well for Fe^{II}-*Cp*Rd failed with Fe^{III}-*Cp*Rd, which suffers from more severe paramagnetic line broadening. No signals were observed in the difference decoupling experiment, and, with the exception of Thr5 and Val38, no additional cross peaks were detected in the paramagnetic-optimized $^{13}C[^{13}C]$ SW-CT-COSY experiment.

The strategy used to assign ^{13}C signals from Fe^{III}-*Cp*Rd took advantage of the complete assignments for Fe^{II}-*Cp*Rd. Titration of the *Cp*Rd with sodium dithionite under normal solution conditions (50 mM phosphate buffer, pH 6.0, 298 K) showed separate sets of peaks from Fe^{II}-*Cp*Rd and Fe^{III}-*Cp*Rd (data not shown). It has been reported that negatively charged residues on the surface of *Cp*Rd hinder protein:protein collisions that lead to electron self-exchange.[35] We added 1 M NaCl to reduce the electrostatic repulsion and increased the sample temperature from 298 to 303 K to increase the collision rate. Under these conditions, a single set of carbonyl ^{13}C peaks was observed, and it was possible to trace the signals from Fe^{III}-*Cp*Rd as the protein was reduced to their assigned positions in Fe^{II}-*Cp*Rd. All the peaks shifted toward their diamagnetic positions as the protein was reduced (Figure 4), as expected because Fe^{II}-*Cp*Rd has a fewer number of unpaired electrons than Fe^{III}-*Cp*Rd. All peaks exhibited exchange broadening in the middle of the redox titration.

Peaks 1 and 2, which overlap in the spectrum of Fe^{II}-*Cp*Rd, had been assigned ambiguously to Thr7/Pro40. Although peaks 1 and 2 could be traced to well-resolved peaks in Fe^{III}-*Cp*Rd,
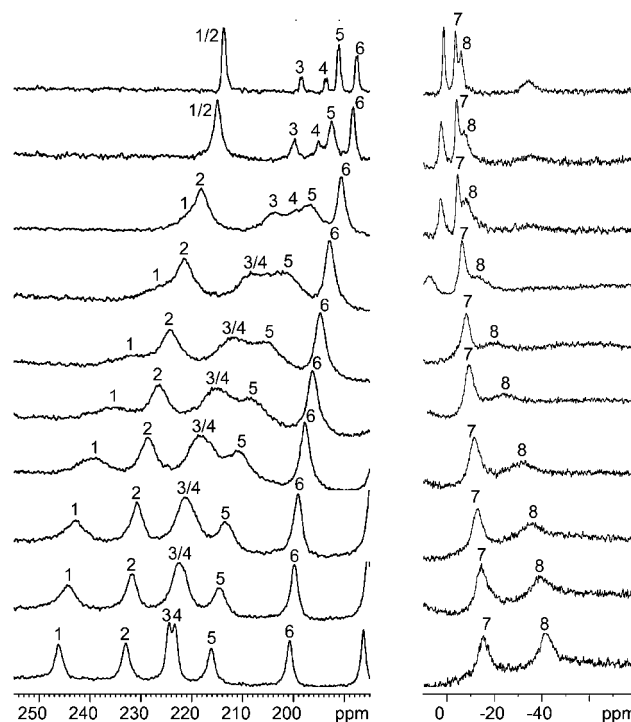
Figure 4. 1D ^{13}C spectra of [U−^{13}C, U−^{15}N]-*Cp*Rd with different concentrations of added sodium dithionite. *Cp*Rd was titrated from the oxidized state (bottom) to the reduced state (top). The numbers correspond to peaks tracked between the oxidized and reduced states of the protein (see text).

the assignment ambiguity remained. Peak 3 (assigned to Thr5) and peak 4 (assigned to Val38) in Fe^{II}-*Cp*Rd, merged in the redox titration and could not be tracked individually. However, it could be deduced from the paramagnetic-optimized $^{13}C[^{13}C]$ SW-CT-COSY spectrum of Fe^{III}-*Cp*Rd and the conventional $^{13}C[^{13}C]$ CT-COSY spectrum of Fe^{II}-*Cp*Rd that, in both oxidation states, the peak at higher frequency is from a threonine spin system and the peak at lower frequency is from a valine spin system. Thus, peaks 3 and 4 were assigned unambiguously in the oxidized state. Peaks 5 and 6, which had been assigned

Table 1. Summary of Hyperfine Shifts Assignments for Fe^{II}-*Cp*Rd[a]

residue	^{15}N	^{13}C′	^{13}C$^{\alpha}$	^{13}C$^{\beta}$	others
Thr5	125[c]	200	73.4	73.0	C$^{\gamma}$ 21.6
Cys6	322	<u>147/147</u>[b]	1234/1124/686	339/−42/−780	
Thr7	279	216	64.0	72.6	C$^{\gamma}$ 22.6
Val8	498	181	63.6	−0.5	C$^{\gamma 1}$ 42.9, C$^{\gamma 2}$ 20.7
Cys9	−1	153[b]	637	−976	
Gly10	222	192	45.5		
Tyr11	394	175	55.6	−6.7	C$^{\gamma}$ 130
Val38	123[c]	195	70.8	37.2	C$^{\gamma 1}$ 22.5, C$^{\gamma 2}$ 19.0
Cys39	294	<u>147/147</u>[b]	1234/1124/686	339/−42/−80	
Pro40	278	216	59.1	36.0	C$^{\gamma}$ 25.1, C$^{\delta}$ 134
Leu41	437	179	55.7	61.0	C$^{\gamma}$ 22.7, C$^{\delta 1}$ 44.9, C$^{\delta 2}$ 41.4
Cys42	−25	<u>156</u>[b]	1234/1124/686	339/−42/−780	
Gly43	223	188	48.0		
Val44	270	175	65.3	26.3	<u>C$^{\gamma 1}$</u> −8.7[d]

[a] Underline: assignment by reference to theoretical calculations. [b] Experiments were carried out on a Bruker DMX400; all others were carried out on a Bruker DMX500. [c] Determined in a previous study.[10] [d] Assignment based on spectra shown in the Supporting Information.

Table 2. Summary of Hyperfine Shifts Assignments for Fe^{III}-*Cp*Rd[a]

residue	^{15}N	^{13}C′	others
Thr5	NA	225	C$^{\alpha}$ 93.6, C$^{\beta}$ 70.2, C$^{\gamma 1}$ 20.1
Cys6	613/588	104/96[b]	NA
Thr7	358	246/233	NA
Val8	525	NA	NA
Cys9	−34	104[b]	NA
Gly10	311	216	
Tyr11	187[c]	NA	55.9, −22.5, 159, 140, 122[c]
Val38	NA	224	C$^{\alpha}$ 90.3, C$^{\beta}$ 35.2, C$^{\gamma 1}$ 22, C$^{\gamma}$ 16.7
Cys39	613/588	104/96[b]	NA
Pro40	407	246/233	NA
Leu41	542	NA	NA
Cys42	−79	104/96[b]	NA
Gly43	327	201	
Val44	346	176/166[c]	C$^{\delta 1}$ −52.6[c]

[a] NA: not available. [b] Experiments were carried out on a Bruker DMX400; all others were carried out on a Bruker DMX500. [c] Assignment based on spectra shown in the Supporting Information.

to Gly10 and Gly43, respectively, in the reduced state, remained well resolved throughout the titration, leading to clear assignments in the oxidized state.

Peaks 7 and 8, which were separately resolved in ^{13}C NMR spectra of the oxidized state, were traced to overlapped signals in the reduced state (Figure 4). Peak 7 was resolved in the paramagnetic optimized ^{13}C[^{13}C] SW-CT-COSY spectrum of Fe^{II}-*Cp*Rd, which correlated this peak to a carbon signal at 130.1 ppm. Combining this result with the paramagnetic-optimized ^{13}C spectra of [^{13}C-Tyr]-*Cp*Rd in both oxidation states (Supporting Information S1), peak 7 was assigned to C$^{\beta}$ of Tyr11. Although peak 8 was not observed in the ^{13}C[^{13}C] SW-CT-COSY spectrum of Fe^{II}-*Cp*Rd, it appeared in the paramagnetic-optimized ^{13}C spectra of [^{13}C-Val]-*Cp*Rd in both oxidation states (Supporting Information S1). Given the exhaustive assignment of ^{13}C signals from paramagnetic residue Val8 and semi-paramagnetic residue Val38 in the reduced state, peak 8 was assigned to the previously unassigned ^{13}C$^{\gamma 1}$ of Val44. The assignments for Fe^{II}-*Cp*Rd are collected in Table 1, and those for Fe^{III}-*Cp*Rd are in Table 2.

Theoretical Calculations of Hyperfine Chemical Shifts and Their Use in Extending Assignments. We previously used hybrid density functional methods to calculate the hyperfine ^{13}C chemical shift values for the four cysteine residues that are covalently bonded to the iron in reduced and oxidized *Cp*Rd.[14]

These calculations were based on a three-dimensional model of atom positions for the residues around the iron center derived from the X-ray structure of the oxidized protein 5RXN.[29] The calculations assumed that the dominant contribution to the hyperfine shift was from Fermi-contact (electron−nuclear) interactions. We have recalculated the chemical shifts of all ^{13}C, and ^{15}N nuclei in the vicinity of the iron in reduced *Cp*Rd on the basis of two models (1FHM and alt-1FHM) from X-ray structure of the reduced protein, which appeared more recently[55] (Table 3); we also have recalculated chemical shifts for ^{13}C and ^{15}N nuclei of the oxidized protein on the basis of the X-ray structure (5RXN) (Table 4). The calculated shifts reported in Tables 3 and 4 are the sum of the calculated Fermi-contact shifts and the mean diamagnetic shifts of the residues from BMRB.

We next evaluated the calculated chemical shifts in light of the available assignments and to consider using the predictions to assign the remaining unassigned signals. Eight broad peaks were detected at abnormal frequencies in the 1D ^{13}C spectrum of reduced [U−^{13}C, U−^{15}N]-*Cp*Rd (Figure 5A). The peaks move toward their diamagnetic positions with increasing temperature as expected for Curie-type electron−nuclear interactions, and these eight signals were predicted to be from the ^{13}C$^{\alpha}$ and ^{13}C$^{\beta}$ atoms of the four ligand cysteines.[14] Subsequent spectra of [^{13}C$^{\beta}$-Cys]-*Cp*Rd confirmed that four of the signals correspond to ^{13}C$^{\beta}$ atoms of cysteines. In the present study, the ^{13}C spectrum of reduced chemically synthesized [^{13}C,^{15}N-Cys9]-*Cp*Rd showed two broad peaks at 637 and −976 ppm (Figure 5B and C) that match the predicted chemical shifts for Cys9 ^{13}C$^{\alpha}$ (647 ppm) and ^{13}C$^{\beta}$ atoms (−928 ppm). We thus assign the peak at −976 ppm to the ^{13}C$^{\beta}$ of Cys9 and the peak at 647 ppm to the ^{13}C$^{\alpha}$ of Cys9 of Fe^{II}-*Cp*Rd. The signals from the other cysteine residues, although they do not exactly match the calculated values, are highly similar to them.

The 1D ^{13}C spectrum of *oxidized* [^{13}C′-Cys]-*Cp*Rd exhibited broad and overlapped signals from the four cysteinyl carbonyl carbons (Figure 5D). The 1D ^{13}C spectrum of oxidized [^{13}C,^{15}N-Cys9]-*Cp*Rd indicated the position of carbonyl carbon from Cys9 to be under the large peak at 104 ppm. By contrast, the 1D ^{13}C spectrum of *reduced* [^{13}C′-Cys]-*Cp*Rd (Figure 5E) exhibited four peaks with different properties: two of them have hyperfine shifts to higher frequency and relax more rapidly, and the other two have hyperfine shifts to lower frequency and relax more slowly. The ^{13}C spectrum of reduced [^{15}N,^{13}C-Cys9]-*Cp*Rd indicated that the carbonyl carbon of residue Cys9 is at 152.8 ppm and has a fast relaxation rate. It is noted that Cys9 and

Table 3. Comparison of Calculated and Experimental ¹³C Shifts for Reduced *Cp*Rd

residue	atom	calculated shift (/ppm) 1FHM	calculated shift (/ppm) alt-1FHM	experimental shift (/ppm)
Thr5	C′	191	193	200
	Cα	82.8	87.4	73.4
	Cβ	71.9	71.9	73.0
	Cγ2	21.5	21.5	21.6
Cys6	C′	145	145	147[a]
	Cα	1496	1611	1234[a]
	Cβ	330	261	339[a]
Thr7	C′	211	214	216
	Cα	64.5	64.5	64.00
	Cβ	74.2	74.2	72.6
	Cγ2	21.5	21.5	22.6
Val8	C′	176	176	181
	Cα	60.2	60.2	63.6
	Cβ	12.0	12.0	−0.50
	Cγ1	62.8	65.0	42.9
	Cγ2	21.3	21.3	20.7
Cys9	C′	150	152	153
	Cα	441	512	637
	Cβ	−930	−838	−976
Gly10	C′	188	190	192
	Cα	40.8	40.8	45.5
Tyr11	C′	175	178	175
	Cα	58.1	58.1	55.6
	Cβ	−2.02	7.15	−6.70
	Cγ	136	140	130
Val38	C′	185	189	195
	Cα	133	89.2	80.9
	Cβ	37.2	37.2	32.7
	Cγ1	22.5	22.5	21.5
	Cγ2	19.0	19.0	21.3
Cys39	C′	136	143	147[a]
	Cα	1237	1230	1124[a]
	Cβ	−78.4	27.1	−42.0[a]
Pro40	C′	230	220	216
	Cα	51.8	54.1	59.1
	Cβ	36.4	36.4	36.0
	Cγ	22.6	22.6	25.1
	Cδ	179	179	134
Leu41	C′	177	172	179
	Cα	51.1	48.8	55.7
	Cβ	39.9	46.8	61.0
	Cγ	24.4	40.5	22.7
	Cδ1	45.2	495	44.9
	Cδ2	24.1	272	41.4
Cys42	C′	147	156	156[a]
	Cα	751	679	686[a]
	Cβ	−719	−534	−780[a]
Gly43	C′	176	179	188
	Cα	45.4	43.1	48.0
Val44	C′	176	176	175
	Cα	69.4	69.4	65.3
	Cβ	21.19	23.48	26.30
	Cγ2	−128	−105	−8.70[a]

[a] Signals tentatively assigned by maximum parsimony.

Table 4. Comparison of Calculated and Experimental ¹³C Shifts for Oxidized *Cp*Rd

residue	atom	calculated shift (/ppm) model 5RXN	experimental shift (/ppm)
Thr5	C′	225	225
	Cα	[a]	93.6
	Cβ	[a]	70.2
Cys6	C′	132	104/96[b]
Thr7	C′	225	233[c]
Val8	C′	170	166[c]
Cys9	C′	124	104
Gly10	C′	220	216
Tyr11	Cβ	−54.4	−22.5
Val38	C′	227	224
Pro40	C′	246	246[c]
Cys42	C′	113	104/96[b]
Gly43	C′	187	201
Val44	C′	176	176[c]
	Cγ1	−32.2	−52.6

[a] Not calculated. [b] Signals were not assigned to individual atoms owing to the relatively small chemical shift differences. [c] Signals assigned by maximum parsimony.
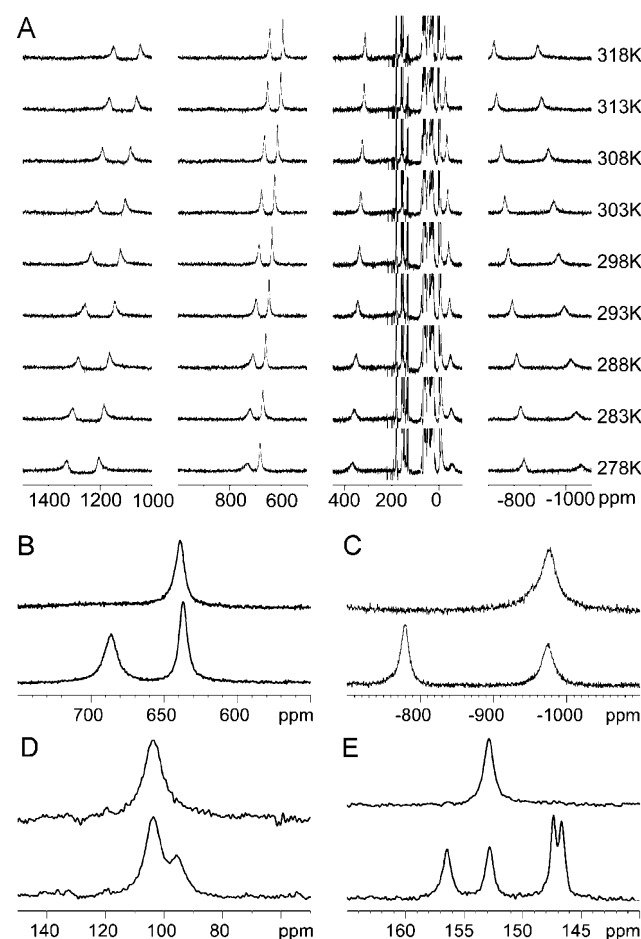
Figure 5. (A) 1D ¹³C spectra of reduced [U−¹³C, U−¹⁵N]-*Cp*Rd at different temperatures listed at the right. (B and C) 1D ¹³C spectra of (bottom) reduced [U−¹⁵N,U−¹³C]-*Cp*Rd and (top) reduced [¹⁵N,¹³C-Cys9]-*Cp*Rd. (D) 1D ¹³C spectra of (bottom) oxidized [¹³C′-Cys]-*Cp*Rd and (top) oxidized [¹⁵N,¹³C-Cys9]-*Cp*Rd. (E) 1D ¹³C spectra of (bottom) reduced [¹³C′-Cys]-*Cp*Rd and (top) reduced [¹⁵N,¹³C-Cys9]-*Cp*Rd. The sample contained 4−8 mM protein, 50 mM potassium phosphate buffer, and 10% ²H₂O; the pH was 6.0, and the temperature was 298 K.

Cys42 are solvent exposed and Cys6 and Cys39 are buried inside *Cp*Rd. In addition, the Sγ atoms of Cys6 and Cys39 each form two H-bonds with other residues; however, the Sγ atoms of Cys9 and Cys42 each only participate in one H-bond. Thus Cys9 and Cys42 fall in one category and Cys6 and Cys39 fall in another category. Hence, it is predicted that the peak at 156.4 ppm belongs to Cys42 and two sharper peaks at lower frequencies are from Cys6 and Cys39.

Overall Agreement between the Assigned and Calculated Chemical Shifts. The set of assigned experimental chemical shifts are compared with Fermi-contact shifts calculated from available X-ray structures in Table 3 for reduced *Cp*Rd and in

Table 4 for oxidized *Cp*Rd. In the two models for reduced *Cp*Rd used in the quantum chemical calculations (Table 3), the side chain of Leu 41 is found in two distinct conformations (1FHM
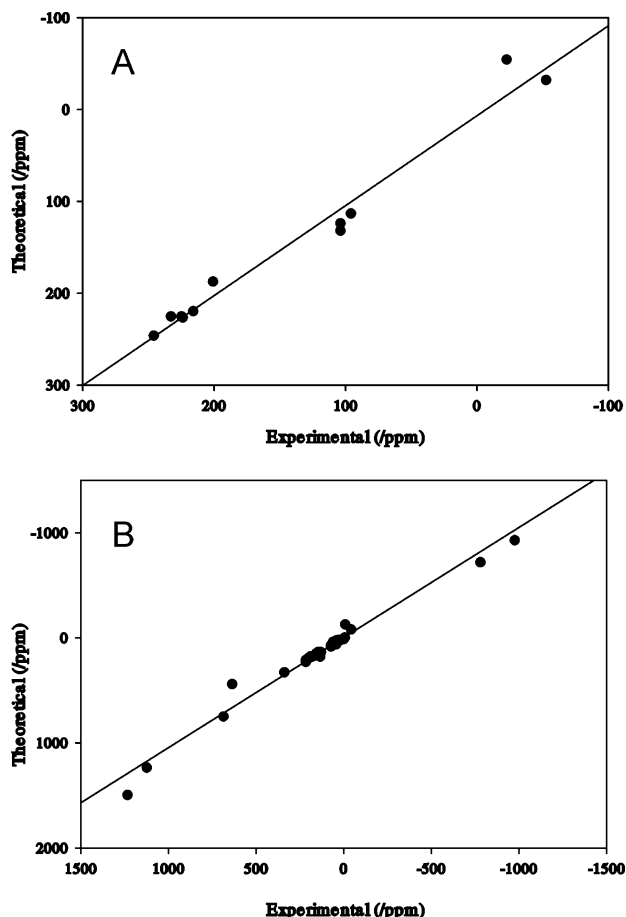
Figure 6. Plots of the theoretical versus experimental chemical shifts for the hyperfine shifted ^{13}C resonances in CpRd. (A) Oxidized CpRd (calculation based on 5RXN model): regression analysis gave an r^2 of 0.98, a slope of 1.01, and an intercept of 0.93. (B) Reduced CpRd (calculation based on 1FHM model): regression analysis gave an r^2 of 0.98, a slope of 1.05, and an intercept of −2.4.

and alt-1FHM).[55] Overall agreement between the experimental and calculated shifts was better for the 1FHM model with Leu 41 in the "open" conformation (rmsd 7.4 ppm) than for the 1FHM-alt model with Leu in the "closed" conformation (rmsd 14 ppm). The largest deviations between the calculated chemical shift based on the two models were for Leu41: whereas the chemical shifts calculated from the 1FHM model showed small deviations from the experimental values (1.7 ppm for Leu41C$^\gamma$, 0.3 ppm for Leu41C$^{\delta1}$, and 17.3 ppm for Leu41C$^{\delta2}$), those from the 1FHM-alt model showed huge deviations (18 ppm for Leu41C$^\gamma$, 450 ppm for Leu41C$^{\delta1}$, and 231 ppm for Leu41C$^{\delta2}$).

For oxidized CpRd, the overall agreement between experimental and calculated (on the basis of the 5RXN model) chemical shifts was quite good (rmsd 4.4 ppm). Figure 6 contains plots of the theoretical versus experimental chemical shifts for the hyperfine shifted ^{13}C resonances in oxidized and reduced CpRd: The computed r^2 values (0.98 in both cases) indicate that the fits are of high quality. Hyperfine calculations of the ^{15}N chemical shifts were reported previously.[14]

Discussion

The current set of ^{13}C and ^{15}N assignments provides a new benchmark for future investigations into the origins of observed hyperfine shifts and their functional significance. Signals from several ^{13}C nuclei with largest calculated hyperfine shifts were

not observed experimentally in the present study, presumably because they are extremely broad. These signals may be candidates for observation by solid state NMR spectroscopy. Paramagnetic restraints (e.g., pseudocontact shifts, paramagnetic relaxation and residual dipolar coupling) are of great use in modern structure determinations.[57,58] Recently, diamagnetic proteins have been engineered to bind paramagnetic tags for the purpose of obtaining paramagnetic restrains.[46,59−63] In spite of the wide application of paramagnetic NMR, with few exceptions,[64,65] detailed analysis has been limited to nuclei ≫5 Å from the metal. The methods presented here that have proved successful with a difficult case having slow electronic relaxation and a high spin metal may be applicable to other metalloproteins.

^{15}N signals were resolved from and assigned to all residues in the two hexapeptide metal-binding loops of reduced CpRd. With the exception of the aromatic carbons from Tyr11, ^{13}C signals were assigned to all carbon atoms from noncysteine residues in the metal-binding loops. Although the direct assignments to cysteinyl carbons were complete only for Cys9, the remaining cysteinyl carbonyl carbon signals were assigned tentatively on the basis of theoretical calculations.

NMR spectra of the oxidized protein (Fe^{III}-CpRd) were much more difficult to collect and analyze than those for the reduced protein (Fe^{II}-CpRd), because of broader lines and more rapidly relaxing signals. Despite this, all hyperfine-shifted ^{15}N signals were resolved and given sequence-specific assignments, with the exception of those from Cys6/Cys39, which remained ambiguously assigned. The ^{13}C signals from Thr5, Val38, Gly10 and Gly43 were clearly assigned. Signals from the carbonyl carbons of Pro40/Thr7 were identified but remained ambiguously assigned. Importantly, signals from the carbonyl carbons of all four cysteine residues were assigned ambiguously.

Assigned hyperfine signals are of great utility in understanding the functional properties of iron−sulfur proteins. Each hyperfine signal characterizes the interplay of a specific nucleus and the delocalized unpaired electrons of the center. Both the chemical shifts and relaxation rates of the hyperfine signals provide information about electron delocalization. Thus, hyperfine signals serve as "fingerprints" of the protein in the vicinity of iron−sulfur cluster. In addition, it has been shown that a change in NH···S$^\gamma$ bond length of only 0.1 Å changes the ^{15}N hyperfine shifts by nearly 90 ppm in oxidized CpRd.[14] Thus, hyperfine shifts offer a measure of lengths of H-bonds to the iron−sulfur cluster with remarkable sensitivity. The present work on assigning ^{13}C and ^{15}N hyperfine signals of CpRd provides the underlying framework for understanding the active site of this protein and establishes a protocol for assigning hyperfine signals from other iron−sulfur proteins. The results clearly show that

(57) Bertini, I.; Luchinat, C.; Parigi, G.; Walker, F. A. *J. Biol. Inorg. Chem.* **1999**, *4*, 515–519.
(58) Hansen, D. F.; Led, J. J. *Proc. Natl. Acad. Sci. U.S.A.* **2006**, *103*, 1738–1743.
(59) Ma, C.; Opella, S. J. *J. Magn. Reson.* **2000**, *146*, 381–384.
(60) Feeney, J.; Birdsall, B.; Bradbury, A. F.; Biekofsky, R. R.; Bayley, P. M. *J. Biomol. NMR* **2001**, *21*, 41–48.
(61) Prudencio, M.; Rohovec, J.; Peters, J. A.; Tocheva, E.; Boulanger, M. J.; Murphy, M. E.; Hupkes, H. J.; Kosters, W.; Impagliazzo, A.; Ubbink, M. *Chemistry* **2004**, *10*, 3252–3260.
(62) Wohnert, J.; Franz, K. J.; Nitz, M.; Imperiali, B.; Schwalbe, H. *J. Am. Chem. Soc.* **2003**, *125*, 13338–13339.
(63) Song, J.; Guo, L. W.; Muradov, H.; Artemyev, N. O.; Ruoho, A. E.; Markley, J. L. *Proc. Natl. Acad. Sci. U.S.A.* **2008**, *105*, 1505–1510.
(64) Babini, E.; Bertini, I.; Capozzi, F.; Felli, I. C.; Lelli, M.; Luchinat, C. *J. Am. Chem. Soc.* **2004**, *126*, 10496–10497.
(65) Bertini, I.; Capozzi, F.; Luchinat, C.; Piccioli, M.; Vila, A. J. *J. Am. Chem. Soc.* **1994**, *116*, 651–660.

1FHM is clearly superior to alt-1FHM as a model for the solution conformation of *Cp*Rd.

Many of the calculated chemical shifts showed remarkable agreement with experiment: of the calculated shifts for reduced *Cp*Rd based on 1FHM, 53% agreed within 0−5 ppm and 26% agreed within 5−20 ppm; of the calculated shifts; for oxidized *Cp*Rd, 46% agreed within 0−5 ppm and 23% agreed within 5−20 ppm. On the other hand, outliers between calculated and experimental shifts were as large as 262 ppm for reduced *Cp*Rd and 32 ppm for oxidized *Cp*Rd. It appears that some regions of the solution structure are not accurately represented by the X-ray models. One such region is the side chain of Val44 which is an outlier in both oxidized and reduced *Cp*Rd. The side chain of residue 44 is known to be critically important in setting the redox potential of the protein.[34,40] Thus, it will be of future interest to use hyperfine shifts for local refinement of the X-ray models.

Supporting Information Available: NMR spectra of oxidized and reduced [U−^{13}C-Val]-*Cp*Rd and oxidized and reduced [U−^{13}C-Tyr]-*Cp*Rd. This material is available free of charge via the Internet at http://pubs.acs.org.

JA905928X